An efficient high-order algorithm for acoustic scattering from penetrable thin structures in three dimensions

Akash Anand[a)]
Applied and Computational Mathematics, California Institute of Technology, Pasadena, California 91125

Fernando Reitich[b)]
School of Mathematics, University of Minnesota, Minneapolis, Minnesota 55455

(Received 6 December 2005; revised 10 February 2007; accepted 13 February 2007)

This paper presents a high-order accelerated algorithm for the solution of the integral-equation formulation of volumetric scattering problems. The scheme is particularly well suited to the analysis of "thin" structures as they arise in certain applications (e.g., material coatings); in addition, it is also designed to be used in conjunction with existing low-order FFT-based codes to upgrade their order of accuracy through a suitable treatment of material interfaces. The high-order convergence of the new procedure is attained through a combination of changes of parametric variables (to resolve the singularities of the Green function) and "partitions of unity" (to allow for a simple implementation of spectrally accurate quadratures away from singular points). Accelerated evaluations of the interaction between degrees of freedom, on the other hand, are accomplished by incorporating (two-face) equivalent source approximations on Cartesian grids. A detailed account of the main algorithmic components of the scheme are presented, together with a brief review of the corresponding error and performance analyses which are exemplified with a variety of numerical results. © *2007 Acoustical Society of America.* [DOI: 10.1121/1.2714919]

PACS number(s): 43.20.Fn, 43.30.Ft [TDM] Pages: 2503–2514

I. INTRODUCTION

The evaluation of scattering returns from large three-dimensional penetrable scatters continues to constitute one of the most challenging problems in computational science. The main difficulties that are present in the problem arise from the need to accurately describe and manipulate highly oscillatory functions. Although a large body of work has been devoted to the subject, scattering problems still cannot be considered completely solved, particularly from a computational perspective, and they remain the subject matter of much ongoing research. A main reason for this lies in the dependence of the mathematical formulation and computational complexities on the oscillations of the incident radiation and on the geometrical and acoustical (or other physical and/or material properties, as the case might be) specifics of the scatterer. The latter include, for instance, their geometrical shapes and material densities, velocities, absorption, and penetrability characteristics, to name but a few.

This diversity of parameters and the different nature of the difficulties associated with particular instances make the case for specialized, application specific algorithms. One such important instance is that of scattering by three-dimensional "thin" scatterers. Thin (thickness up to the order of the wavelength of the incoming radiation) scatterers are used, for instance, to model coatings. Clearly, these have a wide range of practical applications, both for civilian and military purposes (e.g., decoy detection, stealth technology, etc). In this paper, we present a new, efficient and high-order solver for the prediction of the acoustic response of such thin (and possibly inhomogeneous) structures, that is based on the integral equation formulation of the scattering problem. As we explain in the following, and beyond their intrinsic interest and applicability, our new schemes can also be viewed as providing a mechanism to upgrade current low-order (e.g., FFT-based) solvers to fast high-order schemes in the presence of material discontinuities.

Most existing algorithms for computing solutions to volumetric scattering problems can be broadly classified into three classes, depending on the underlying mathematical formulation of the problem: (i) Differential equation methods; (ii) variational methods; and (iii) integral equation methods. The methods in category (i) are based on direct discretization of the differential equation [e.g., Eq. (1)] and they include, most notably, finite difference schemes (e.g., FDTD techniques[1–3]). Those in category (ii), in contrast, work with the variational form of the equation, such as in all variants of the finite element (FE) method.[4–6] In both cases, however, a central challenge facing these numerical procedures in connection with scattering applications relates to the need to truncate the (infinite) physical domain. This issue has received, and continues to receive, significant attention in the literature as the imposition of approximate absorbing or transparent boundary conditions, or the use of perfectly matched layers (PML), can still yield, in some cases, unacceptable results. On the other hand, even when an approximate treatment of the truncation boundary/region does not pollute the numerical solution (e.g., when this is effected at a considerable distance from the scatterers), other sources of error may produce unwanted results. In this regards, perhaps the most prominent source can be attributed to the dispersive

[a)]Electronic mail: anand@acm.caltech.edu
[b)]Electronic mail: reitich@math.umn.edu

characteristics of standard (low-order) methods based on differential and variational formulations. A classical remedy resorts to smaller grid spacing, with a consequent increase in computational effort.

A number of more sophisticated solutions to the low accuracy of standard FDTD and/or FE methodologies, however, have been developed. Generically, these algorithms are based on the use of higher-order discretization schemes. Most notable among these are so-called "spectral methods,"[7–11] based on the use of global spatial basis functions, that provide spectral accuracy in the approximation of smooth functions. In the time domain, different methods within this category handle temporal derivatives differently.

For example, the pseudospectral time-domain (PSTD) methods[7,8] use conventional differencing schemes, e.g., leapfrog, to evolve the solution in time. The "k-space method," originally proposed by Bojarski[12,13] and further developed by Mast *et al.*,[10] on the other hand, uses a nonstandard finite difference approach for temporal integration, which is exact for the homogeneous case; spectral approximations in time have also been used.[14]

While extremely efficient and accurate within their domain of applicability, the implementation of spectral methodologies is, however, nontrivial, and their convergence properties, specifically for those based on the more efficient Fourier spectral approximations, are dependent on the underlying material properties. Indeed, for instance, when applied in a straightforward manner, these techniques suffer from so-called "wraparound effects," caused by the lack of periodicity in the problem. As has been recently shown in the context of the PSTD and k-space approaches,[9,11] however, these effects can be significantly mollified by employing a PML. In this manner, and for practical purposes, the resulting schemes can be considered to converge with higher orders, at least in simulations that entail smooth scattering media. The extension to scattering configurations that present material discontinuities, on the other hand, is substantially impeded by Gibbs-type phenomena that are inherent to spectral approximations. The modifications that have been proposed to date to alleviate these effects are not as satisfactory: Those based on filtering[10,11] or NUFFTs[15–17] clearly do not retain high-order convergence characteristics, while those that use postprocessing procedures (e.g., Gegenbauer reconstruction[18]) are of limited applicability[19,20] and, moreover, they can adversely affect the computational cost.

As we mentioned, the work we present here relates to a new methodology for the solution of the (volumetric) integral equation formulation of the scattering problem that provides a high-order treatment of material discontinuities. Our approach, therefore, falls within the above-mentioned category (iii) and, as such, it obviates the need for the explicit imposition of radiation conditions (as these are encoded in the Green's function). Within this class of methods, perhaps the best known algorithms are those related to the CGFFT,[21,22] which uses an iterative procedure (conjugate gradients, in this case) to solve the (convolution) integral equation; at each iteration the convolution is effected with fast Fourier transforms which, for a number N of unknowns, entails a cost of $O(N \log N)$ [instead of the $O(N^2)$ cost of direct evaluation]. Again here, this solution procedure leads to very efficient numerics and is highly accurate for smoothly varying media, but its convergence degrades significantly in the presence of material discontinuities.[17,23] In fact, to our knowledge, only limited attempts have been made toward the development of efficient higher-order integral-equation solvers for volumetric scattering applications. A notable exception is the work of Zhu and Gedney,[24,25] based on the "discontinuous FFT" of Fan and Liu.[23] This latter scheme is based on the accurate evaluation of Fourier coefficients of discontinuous functions (through Gaussian quadratures and careful interpolation from and to equispaced grids) and, while it can be shown that this improves on the convergence of the CGFFT (from first- to second-order accurate, in fact), it fails to address the Gibbs phenomenon which arises as the Fourier series is summed. A simpler and more efficient approach, based on a suitable decomposition of the Green's function, and also leading to second-order convergence for discontinuous scatterers, has been recently proposed in Ref. 26.

The rest of the paper is organized as follows. In Sec. II, we precisely define the concept of a "thin structure" and we review the mathematical formulation of the corresponding volumetric scattering problem, based on the solution of the Helmholtz equation. The main algorithmic components of our approach are detailed in Sec. III. In Sec. IV, an analysis of the accuracy and efficiency of the numerical scheme is presented. This is followed, in Sec. V, by a presentation of the results from a variety of numerical experiments that exemplify the properties of the procedure. We present, in Sec. VI, a brief discussion on the use of our thin volume integrator in conjunction with existing low-order FFT-based methods to upgrade their order of accuracy in the presence of material discontinuity. Finally, our conclusions are summarized in Sec. VII.

II. PRELIMINARIES

A. Mathematical formulation

As mentioned earlier, we shall consider the Helmholtz model of acoustic scattering by a bounded, inhomogeneous medium Ω of refractive index $n(\mathbf{x})$. Within this context, given an incident field u^i, its interaction with the scatterer produces a scattered field u^s and the total field $u=u^i+u^s$, satisfies the Helmholtz equation

$$\Delta u(\mathbf{x}) + \kappa^2 n^2(\mathbf{x}) u(\mathbf{x}) = 0, \quad \mathbf{x} \in \mathbb{R}^3. \tag{1}$$

In addition, the Sommerfeld radiation condition is imposed on u^s to enforce its outgoing character. Equivalently,[27] the total field u also satisfies the Lippmann-Schwinger integral equation

$$u(\mathbf{x}) + \kappa^2 K[u](\mathbf{x}) = u^i(\mathbf{x}), \quad \mathbf{x} \in \mathbb{R}^3, \tag{2}$$

where

$$K[u](\mathbf{x}) = \int_\Omega G(\mathbf{x},\mathbf{x}') m(\mathbf{x}') u(\mathbf{x}') d\mathbf{x}', \tag{3}$$

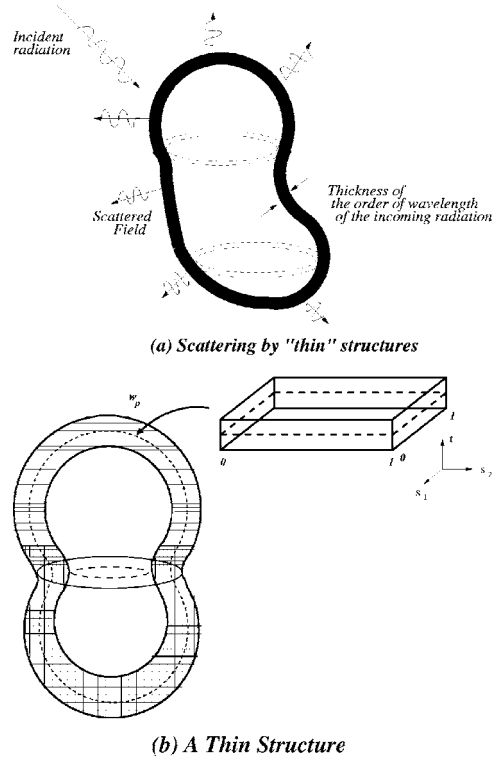

FIG. 1. Description of thin structures; overlapping patches and corresponding parametric spaces are constructed to cover the scatterer of thickness of the order of the wavelength of incoming radiation.

$$G(\mathbf{x},\mathbf{x}') = \frac{\exp(\iota\kappa|\mathbf{x}-\mathbf{x}'|)}{4\pi|\mathbf{x}-\mathbf{x}'|}$$

is the Green's function for the Helmholtz equation in three dimensions and $m=1-n^2$. Note that $m\equiv 0$ outside of Ω and also that the choice of Green's function guarantees that u^s is outgoing. The solvability of the integral equation (2) has been thoroughly investigated, and positive results have been established for rather general contrast functions m; see, e.g., Refs. 27–30

As we said, our initial developments will be geared toward solvers for thin structures which we formally define next.

B. Thin structures

A thin structure Ω (see Fig. 1) is described by a finite collection of patches $\mathcal{P}=\{\mathcal{P}^p : p=1,\ldots,P\}$ that cover the entire structure, i.e., $\Omega=\cup_{p=1}^{P}\mathcal{P}^p$, where each patch is parameterized by a smooth invertible map $\mathbf{x}^p:(0,1)^3\to\mathcal{P}^p$,

$$\mathbf{x}^p = \mathbf{x}^p(\mathbf{s},t), \quad (\mathbf{s},t)=(s_1,s_2,t)\in(0,1)^3.$$

By convention, the two-dimensional variable $\mathbf{s}$ shall correspond to "parallel" coordinates while the variable t will describe the structure in the "transverse" direction. *We say that the structure Ω is thin if the thickness*

$$\sup_{\mathbf{s}\in(0,1)^2} |\mathbf{x}^p(\mathbf{s},1)-\mathbf{x}^p(\mathbf{s},0)| \lesssim \lambda \tag{4}$$

for all $p=1,\ldots,P$. Here, $\lambda=2\pi/\kappa$ is the wavelength of the incident radiation.

III. AN EFFICIENT HIGH-ORDER SOLVER

Naturally, the possibility of producing fast and accurate solutions depends on our ability to evaluate the integral in Eq. (3) accurately and efficiently. Clearly, $G(\mathbf{x},\mathbf{x}')$ changes rapidly when the source point $\mathbf{x}'$ is close to or, in other words, *adjacent* to the target point $\mathbf{x}$ and is singular when $\mathbf{x}=\mathbf{x}'$. Thus, the first difficulty relates to the design of high order quadratures for $K[u](\mathbf{x})$ in the vicinity of the target point $\mathbf{x}$. More precisely, for a neighborhood $\mathcal{N}_\mathbf{x}$ of $\mathbf{x}$, we can separate the integral in Eq. (3) into

$$K[u](\mathbf{x}) = \int_{\mathcal{N}_\mathbf{x}} G(\mathbf{x},\mathbf{x}')m(\mathbf{x}')u(\mathbf{x}')d\mathbf{x}' + \int_{\Omega\setminus\mathcal{N}_\mathbf{x}} G(\mathbf{x},\mathbf{x}')m(\mathbf{x}')u(\mathbf{x}')d\mathbf{x}' \tag{5}$$

corresponding to "adjacent" and "nonadjacent" interactions, respectively; the calculation of the (singular) adjacent interactions then necessitates the design of a specialized quadrature rule (Sec. III A). Once these *adjacent interactions* have been computed, there will only remain to compute nonadjacent interactions

$$\int_{\Omega\setminus\mathcal{N}_\mathbf{x}} G(\mathbf{x},\mathbf{x}')m(\mathbf{x}')u(\mathbf{x}')d\mathbf{x}'.$$

The accurate evaluation of these though does not pose a major difficulty in the design of approximate quadratures as the integrand is regular. However their number [entailing $\mathcal{O}(N)$ operations for each of N target points] demands the design of a suitable "accelerator" (Sec. III B). In summary, the goal is to design an algorithm that accurately evaluates the singular *adjacent interactions* without compromising speed and that can, at the same time, efficiently evaluate the voluminous number of *nonadjacent interactions*.

A. Adjacent interactions

The singular nature of the integral kernel $G(\mathbf{x},\mathbf{x}')$ causes the main difficulty in high-order evaluation of *adjacent interactions*. Even though the use of the well-known strategy of "singularity subtraction" does give rise to bounded integrands, an application of classical high-order quadratures to these still fails to provide high-order results, since the higher order derivatives of the integrand are unbounded. Thus, a specialized quadrature rule must be developed and used to achieve high-order accuracy.

To present the method, consider a partition of unity subordinated to the covering $\mathcal{P}$, that is a collection of functions

$$w^p(\mathbf{x}), \quad p=1,\ldots,P, \tag{6}$$

such that

(1) w^p is defined, smooth, and non-negative in Ω, and it vanishes outside $\mathcal{P}^p$, and
(2) $\Sigma_{p=1}^{P} w^p = 1$ throughout Ω.

Then, we can write

$$K[u](\mathbf{x}) = \sum_{p=1}^{P} K_p[u](\mathbf{x}),$$

where

$$K_p[u](\mathbf{x}) = \int_0^1 \left(\int_{[0,1]^2} G(\mathbf{x}, \mathbf{x}^p(\mathbf{s}',t')) \phi_u^p(\mathbf{s}',t') d\mathbf{s}' \right) dt' \tag{7}$$

and

$$\phi_u^p(\mathbf{s},t) = m(\mathbf{x}^p(\mathbf{s},t)) u(\mathbf{x}^p(\mathbf{s},t)) w^p(\mathbf{x}^p(\mathbf{s},t)) J^p(\mathbf{s},t).$$

Here, J^p is the Jacobian of the transformation $\mathbf{x}^p$.

In the case when $\mathbf{x}$ does not lie on the integration patch $\mathcal{P}^p$, the integrand in Eq. (7) is smooth and as a result can be integrated to high order. The fact that the integrands in the two-dimensional "parallel" integrals

$$\int_{[0,1]^2} G(\mathbf{x}, \mathbf{x}^p(\mathbf{s}',t')) \phi_u^p(\mathbf{s}',t') d\mathbf{s}'$$

vanish to high order at the boundary of the integration domain $[0,1]^2$ (due to the presence of w^p as a factor) suggests the use of trapezoidal rule for the approximation as it is well known to achieve spectral accuracy for such smooth and periodic integrands. Indeed, *(1) for* $\mathbf{x} \notin \mathcal{P}^p$, *use of trapezoidal rule to compute two-dimensional "parallel" integrals and a high-order composite Newton-Cotes quadrature for the transverse integral, on a uniform grid* $(\mathbf{s}_{ij}, t_k) = (ih_{s_1}, jh_{s_2}, kh_t)$ *on the parameter space of* $\mathcal{P}^p$, yields an overall highly accurate numerical quadrature.

On the other hand, the case when $\mathbf{x} = \mathbf{x}^p(\mathbf{s},t)$ lies in the integration patch $\mathcal{P}^p$ needs a more careful treatment if high-order accuracy is to be achieved, due to the singular nature of the integrand in Eq. (7). To this end, we begin by using a smooth cut-off function $\eta_{\mathbf{s}}$ satisfying

$$\eta_{\mathbf{s}}(\mathbf{s}') = 1 \text{ for } |\mathbf{s} - \mathbf{s}'| < r_1, \quad \eta_{\mathbf{s}}(\mathbf{s}') = 0 \text{ for } |\mathbf{s} - \mathbf{s}'| \geqslant r_0, \tag{8}$$

to localize the singularity

$$\begin{aligned} K_p[u](\mathbf{x}) = & \int_0^1 \int_{B(\mathbf{s},r_0)} G(\mathbf{x}, \mathbf{x}^p(\mathbf{s}',t')) \phi_u^p(\mathbf{s}',t') \eta_{\mathbf{s}}(\mathbf{s}') d\mathbf{s}' dt' \\ & + \int_0^1 \int_{[0,1]^2} G(\mathbf{x}, \mathbf{x}^p(\mathbf{s}',t')) \phi_u^p(\mathbf{s}',t') (1 \\ & - \eta_{\mathbf{s}}(\mathbf{s}')) d\mathbf{s}' dt', \end{aligned} \tag{9}$$

where $B(\mathbf{s}, r_0)$ denotes the disc of radius r_0 centered at $\mathbf{s}$. The factor $1 - \eta$ in the integrand of the second integral in Eq. (9) removes the singularity of the Green's function which can, therefore, be integrated to high-order directly as in the above-described case $\mathbf{x} \notin \mathcal{P}^p$, that is

(2) if $\mathbf{x} \in \mathcal{P}^p$, *the integral away from the target point is approximated as in step (1).*

To deal with the first integral, on the other hand, we denote the "parallel" integrals corresponding to each t' by $I_u^p(t';\mathbf{x})$, i.e.,

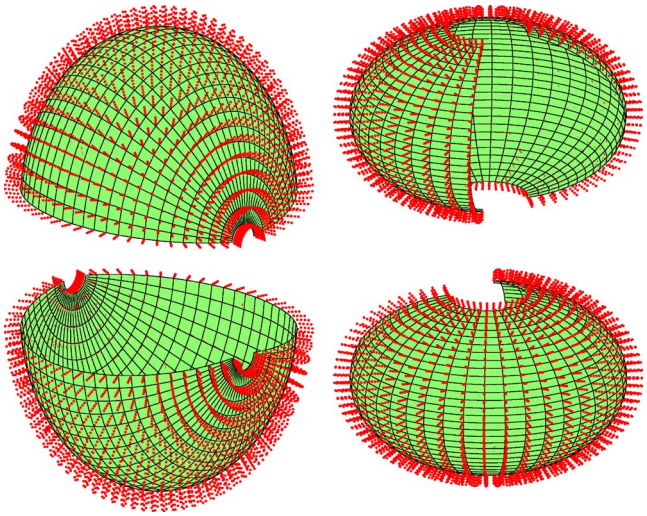

FIG. 2. (Color online) Four patches used to cover the spherical shell and corresponding discretization grids used for the scattering computation.

$$I_u^p(t';\mathbf{x}) = \int_{B(\mathbf{s},r_0)} G(\mathbf{x}, \mathbf{x}^p(\mathbf{s}',t')) \phi_u^p(\mathbf{s}',t') \eta_{\mathbf{s}}(\mathbf{s}') d\mathbf{s}' \tag{10}$$

so that it can be rewritten as

$$\int_0^1 I_u^p(t';\mathbf{x}) dt'. \tag{11}$$

As we anticipated, evaluation of $I_u^p(t';\mathbf{x})$ poses difficulties due to the singular character of integrand for $t = t'$ and the "near singularity" when t' is close to t. To overcome these difficulties, the following twofold strategy is used:

(a) A change to polar coordinates (ρ, θ) around the point $\mathbf{s}$ in the $\mathbf{s}'$ plane, transforms the integral in Eq. (10) to

$$\begin{aligned} I_u^p(t';\mathbf{x}) = & \int_0^{2\pi} d\theta \int_0^{r_0} G(\mathbf{x}, \mathbf{x}^p(\mathbf{s} + \rho \mathbf{d}_\theta, t')) \\ & \times \phi_u^p(\mathbf{s} + \rho \mathbf{d}_\theta, t') \eta_{\mathbf{s}}(\mathbf{s} + \rho \mathbf{d}_\theta, t') \rho d\rho, \end{aligned}$$

where $\mathbf{d}_\theta = (\cos\theta, \sin\theta)$. The additional factor ρ makes possible the use of a uniform grid in θ (independent of ρ and t') for the approximation of the θ integrals, which can be performed accurately using trapezoidal rule in view of the θ-periodic smooth integrands.

(b) Use of an additional change of variables $\rho = \rho(\tau)$ such that

$$\left. \frac{d^m \rho}{d\tau^m} \right|_{\tau=0} = 0 \quad \text{for } m = 0, \ldots, M \tag{12}$$

[e.g., $\rho(\tau) = \tau^{M+1}$] gives

$$I_u^p(t';\mathbf{x}) = \int_0^{2\pi} d\theta \int_0^{\tau_0} \frac{\rho(\tau)\rho'(\tau)}{|\mathbf{x} - \mathbf{x}^p(\mathbf{s} + \rho(\tau)\mathbf{d}_\theta, t')|} f_u^p(\tau, \theta; t') d\tau, \tag{13}$$

where

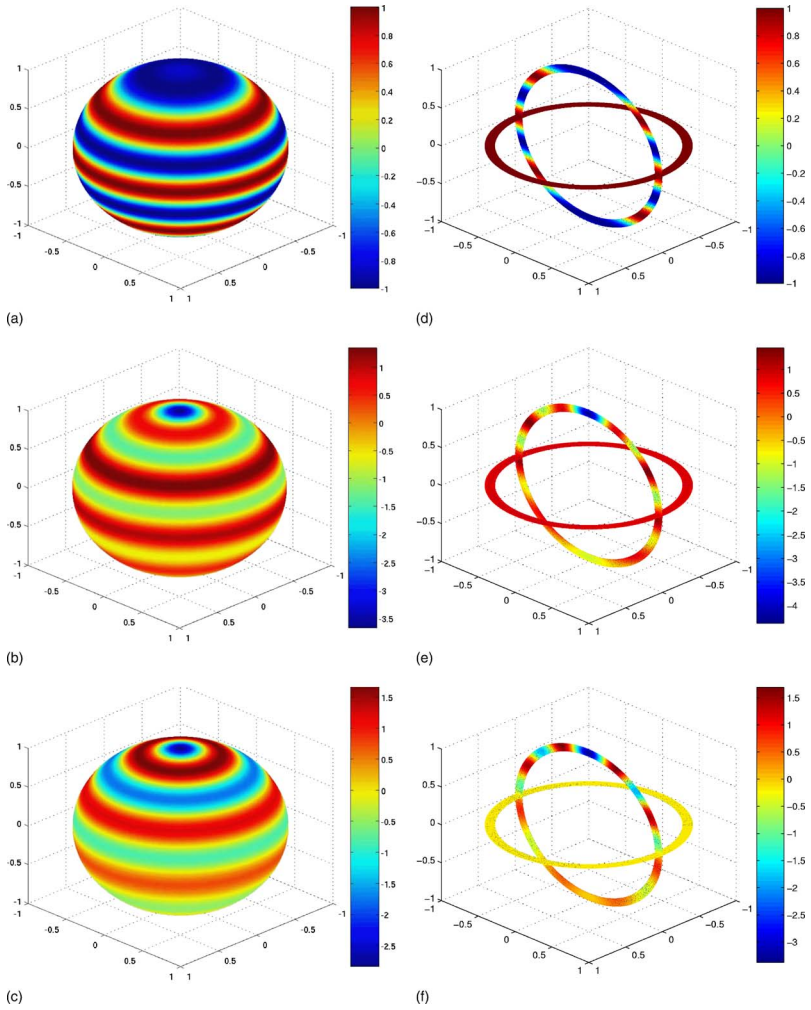

FIG. 3. (Color online) Scattering of an incoming plane-wave by a thin spherical shell. (a), (b), and (c) The surface view of the incident, total, and scattered field, respectively; (d), (e), and (f) the corresponding cross-sectional view.

$$f_u^p(\tau,\theta;t') = \frac{1}{4\pi}\exp(\iota\kappa|\mathbf{x}-\mathbf{x}^p(\mathbf{s}+\rho(\tau)\mathbf{d}_\theta,t')|) \times \phi_u^p(\mathbf{s}+\rho(\tau)\mathbf{d}_\theta,t')\,\eta_{\mathbf{s}}(\mathbf{s}+\rho(\tau)\mathbf{d}_\theta,t')$$

and $\tau_0=\rho^{-1}(r_0)$. The integrand in Eq. (13) now has M derivatives in τ that are uniformly bounded and it also vanishes to high order at the end points $\tau=0$ and $\tau=\tau_0$, so that a high-order integration in τ can be achieved using the trapezoidal rule.

Note that in order to perform the integration in Eq. (13), for each t', we need the density, $\phi_u^p(\mathbf{s}+\rho(\tau)\mathbf{d}_\theta,t')$ on a polar grid $(\tau_{l_1},\theta_{l_2})$ around $\mathbf{s}$ in the $\mathbf{s}'$ plane (a uniform grid in the θ direction and a ρ-transformed grid in the radial direction). In order to obtain this additional data from the original grid $(\mathbf{s}_{ij},t_k)$, we use FFT-refined polynomial interpolation procedure described in the following.

(3) Obtain the Fourier coefficients of the density ϕ_u^p for each of the planes $\{(\mathbf{s},t_k):\mathbf{s}\in(0,1)^2\}$ using two-dimensional fast Fourier transforms, $\mathcal{FFT}(\phi_u^p)$.

(4) Evaluate the Fourier series on a much finer equispaced grid $(\mathbf{s}_{ij}/F,t_k)$, where F is the level of refinement (e.g., $F=2,4,8,\ldots$). These evaluations can be obtained efficiently using two-dimensional fast Fourier transforms, $\mathcal{FFT}^{-1}$. As a result of steps 3 and 4, we achieve a spectrally accurate "trigonometric" interpolation of smooth and periodic density on an F-times finer grid.

(5) *Two-dimensional polynomial interpolation of a fixed order R* (e.g., *bicubic*, $R=4$) *can be performed locally on the fine grid $(\mathbf{s}_{ij}/F,t_k)$ to obtain the interpolated density values on the polar grid $(\tau_{l_1},\theta_{l_2})$*. The resulting FFT-refined polynomial interpolation scheme is much more accurate for our smooth periodic density than a polynomial interpolation alone [as the error is proportional to $(h_{s_1}/F)^R+(h_{s_2}/F)^R$ rather than simply to $h_{s_1}^R+h_{s_2}^R$]. Finally,

(6) *if $\mathbf{x}\in\mathcal{P}^p$ and for integration near the target point, use the interpolated data to evaluate an accurate approximation of the parallel integral (13) in the form of the trapezoidal rule in the transformed variables (τ,θ)*,

$$I_u^p(t';\mathbf{x}) \approx \sum_{l_1,l_2} G(\mathbf{x},\mathbf{x}^p(\mathbf{s}+\rho(\tau_{l_1})\mathbf{d}_{\theta_{l_2}},t')) \times \phi_u^p(\mathbf{s}+\rho(\tau_{l_1})\mathbf{d}_{\theta_{l_2}},t')\,\eta_{\mathbf{s}}(\mathbf{s}+\rho(\tau_{l_1})\mathbf{d}_{\theta_{l_2}},t') \times \rho(\tau_{l_1})\rho'(\tau_{l_1})\Delta\tau\Delta\theta.$$

Finally, the integration in the transverse direction

TABLE I. Convergence study. Plane-wave scattering ($\kappa=10$) by a spherical shell (radius=1; thickness=0.025).

Grid size	Unknowns	Samp. density[a]	$\mathcal{E}$	Order
$4\times16\times16\times5$	5 120	1.6	4.6803×10^{-2}	⋯
$4\times32\times32\times5$	20 480	3.2	1.9998×10^{-3}	4.5487
$4\times64\times64\times5$	81 920	6.4	9.2095×10^{-5}	4.4406
$4\times128\times128\times5$	327 680	12.8	1.7774×10^{-6}	5.6953

[a]Number of points per wavelength.

TABLE II. Computational efficiency. Spherical shell geometry.

κ	Thickness	N	β	$\mathcal{E}$	$\mathcal{R}$
2	0.1	5 120	0.325	1.3121×10^{-3}	⋯
4	0.05	20 480	0.419	7.8718×10^{-4}	3.1
8	0.025	81 920	0.490	8.4803×10^{-5}	3.4
16	0.0125	327 680	0.546	4.4295×10^{-4}	3.8

[t'-direction in Eq. (11)] can be handled through a high-order quadrature rule, if carefully partitioned. Indeed the integrand $I_u^p(t';\mathbf{x})$ is precisely a *single layer potential* supported on the surface

$$S_{t'}=\{\mathbf{x}^p(\mathbf{s}',t'):\mathbf{s}'\in(0,1)^2\}$$

and it is therefore smooth for $0\leqslant t'\leqslant t$ and for $t\leqslant t'\leqslant 1$ (in fact, it has a corner type singularity at $t=t'$[27]). Hence we rewrite Eq. (11) as

$$\int_0^t I_u^p(t';\mathbf{x})dt'+\int_t^1 I_u^p(t';\mathbf{x})dt', \tag{14}$$

where each integrand is smooth and can therefore be treated with a high-order composite Newton quadrature with a number Q of points. To this end, however, we need the values of $I_u^p(t';\mathbf{x})$ at points, say $\tilde{t}_k$, other than the original grid points $\{t_k\}$, to evaluate Eq. (14) when t is near 0 or 1 [so that there are enough data points on the grid between 0 and t or t and 1 to enable a high-order quadrature of the integrands in Eq. (14)]. To obtain these extra values, we pursue the following scheme:

(7) *For each* $\mathbf{s}_{ij}$ *on an equispaced grid, we interpolate the smooth density* $\phi_u^p(\mathbf{s}_{ij},t)$ *to obtain additional values in t-direction at points* $\tilde{t}_k$ *near the end points* $t=0$ *and* $t=1$.

(8) *Perform the parallel local integration in Eq. (13) (again in transformed variables) to obtain the values* $I_u^p(\tilde{t}_k;\mathbf{x})$ *at these additional points*.

Once we have the additional data, we

(9) *evaluate the full local integral (14) with a high-order Newton-Cotes quadrature in the transverse direction*.

As a result, steps 1–9 provide a high-order quadrature for adjacent interactions. As we said, the use of a partition of unity (6) allows for the integration of the (nonsingular) nonadjacent interactions to be performed to high order with a simple use of the trapezoidal rule. There, however, the central issue is one of computational cost; a strategy to reduce this is described in the following.

B. Nonadjacent interactions: Acceleration

As we noted in Sec. III A, difficulties in integration arise only when the source point is close to the target point [due to the behavior of the kernel $G(\mathbf{x},\mathbf{x}')$]. The above-described integration scheme for adjacent interactions is unnecessary for source points that are sufficiently away from the target point and, in fact, a more efficient strategy can be devised. Indeed, for these, a direct application of the trapezoidal rule yields superalgebraic convergence, on account of the smooth vanishing of the functions $w^p(\mathbf{x})$ in Eq. (6). However such a procedure results in an $\mathcal{O}(N^2)$ algorithm which may be suitable only for relatively small N. For large N, on the other hand, we propose a variant of the acceleration strategy introduced in Ref. 31, for surface scattering that is suitable to our volumetric problem.

Specifically, as in Ref. 31, our acceleration strategy is based on certain distributions of "equivalent sources" on Cartesian grids. More precisely, we begin by bounding the obstacle by a cube $\mathcal{C}$ of side length A which is then partitioned into L^3 identical cubes $\mathcal{C}_i$ of side $H=A/L$.

We then replace the true sources contained in the cube $\mathcal{C}_i$ by a number M^{equiv} of "equivalent sources" on the faces of $\mathcal{C}_i$ in such a way that the field produced by these equivalent sources coincides, to high-order accuracy, with the field generated by the "true sources" (volume discretization data) in $\mathcal{C}_i$ at all points in space that are "not adjacent" to $\mathcal{C}_i$. Three independent sets $\mathcal{F}_i^l$, $l=1,2,3$ of equivalent sources, comprising both monopoles of intensity $\xi_{i,j}^l$ ($\xi_{i,j}^l G(\mathbf{x},\mathbf{x}_{i,j}^l)$) and dipoles of intensity $\zeta_{i,j}^l$ ($\zeta_{i,j}^l \partial G(\mathbf{x},\mathbf{x}_{i,j}^l)/\partial x_l$), are used for this calculation. These equivalent sources in $\mathcal{F}_i^l$ are placed on an equispaced grid $\mathbf{x}_{i,j}^l$, $j=1,\ldots,M^{\text{equiv}}$ on the union of two faces of $\mathcal{C}_i$ that are parallel to coordinate plane $x_l=0$. The field generated by these equivalent sources

$$K_{na,\text{eq}}^{l,\mathcal{C}_i}[u](\mathbf{x})=\sum_{j=1}^{(1/2)M^{\text{equiv}}}\left(\xi_{i,j}^l G(\mathbf{x},\mathbf{x}_{i,j}^l)+\zeta_{i,j}^l\left.\frac{\partial G(\mathbf{x},\mathbf{x}')}{\partial x_l'}\right|_{\mathbf{x}'=\mathbf{x}_{i,j}^l}\right) \tag{15}$$

approximates the field generated by true sources in $\mathcal{C}_i$ within

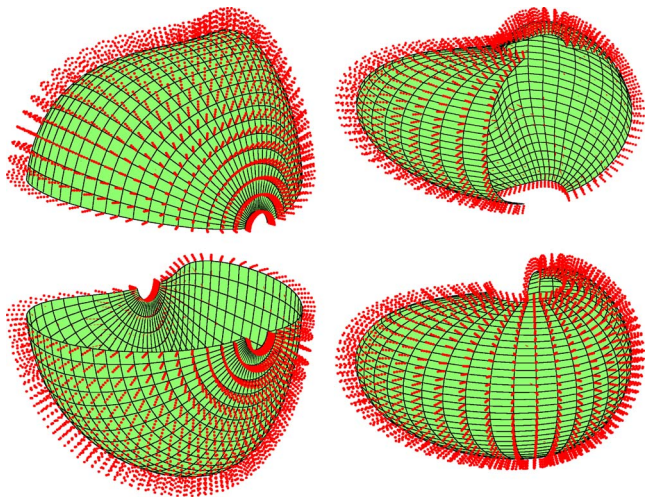

FIG. 4. (Color online) Patches used for the bean shaped scattering geometry and corresponding discretization grids for computation.

a prescribed tolerance ϵ, provided M^{equiv} is chosen as[31]

$$M^{\text{equiv}} = \max\left\{\frac{4\kappa^2 A^2}{L^2}, 4c^2(\epsilon)\right\}, \tag{16}$$

where

$$c(\epsilon) = -\frac{\log(\epsilon)}{\log(3)}.$$

Denoting the field generated by the true sources within the cell $\mathcal{C}_i$ by $K^{\mathcal{C}_i}_{\text{true}}[u](\mathbf{x})$, the intensities $\xi^l_{i,j}$ and $\zeta^l_{i,j}$ are then chosen such that the vector formed by the differences $(K^{\mathcal{C}_i}_{\text{true}}[u](\mathbf{x}) - K^{l,\mathcal{C}_i}_{na,\text{eq}}[u](\mathbf{x}))$ is minimized in the mean-square norm as $\mathbf{x}$ varies over a number $n^{\text{coll}} \approx 2M^{\text{equiv}}$ collocation points on $\partial\mathcal{S}_i$, where the "supercube" $\mathcal{S}_i$ is union of $\mathcal{C}_i$ and its neighboring cells. Thus (for stability reasons) these intensities are obtained as the least-squares solution of an overdetermined linear system.

Now, recalling the definitions of adjacent and nonadjacent interactions, and replacing $\mathcal{N}_{\mathbf{x}}$ in Eq. (5) with $\mathcal{S}_i$, we have for $\mathbf{x} \in \mathcal{C}_i$,

$$K[u](\mathbf{x}) = K_a[u](\mathbf{x}) + K_{na}[u](\mathbf{x}),$$

where

$$K_a[u](\mathbf{x}) = \int_{\mathcal{S}_i} G(\mathbf{x},\mathbf{x}')m(\mathbf{x}')u(\mathbf{x}')d\mathbf{x}' \tag{17}$$

and

$$K_{na}[u](\mathbf{x}) = \int_{\dot{\Omega}\setminus\mathcal{S}_i} G(\mathbf{x},\mathbf{x}')m(\mathbf{x}')u(\mathbf{x}')d\mathbf{x}'. \tag{18}$$

For each $l=1,2,3$, we define

$$K^l_{na,\text{eq}}[u](\mathbf{x}) = \sum_{i=1}^{L^3} K^{l,\mathcal{C}_i}_{na,\text{eq}}[u](\mathbf{x}) - \sum_{\{i|\mathcal{C}_i\subset\mathcal{S}_i\}} K^{l,\mathcal{C}_i}_{na,\text{eq}}[u](\mathbf{x}), \tag{19}$$

which provide accurate approximations to $K_{na}[u]$ throughout the boundary of each cell $\mathcal{C}_i$. The key observation here, of course, is that both summations in Eq. (19), being exact convolutions on a Cartesian grid, can be evaluated efficiently by means of fast Fourier transforms.

Finally, the evaluation of the field values at the true source location from its values at the boundaries of each cell $\mathcal{C}_i$ amounts to solving (Dirichlet) boundary value problems within each $\mathcal{C}_i$. Such Dirichlet problems can be solved uniquely and in a stable manner since the size of the cells can be chosen so that internal resonances do not occur.[31] For efficiency, the field values inside a cell are obtained using a discretized plane wave expansion,[32]

$$K_{na,\text{eq}}[u](\mathbf{x}) = \sum_{k=1}^{n^{\text{wave}}} \psi_k \exp(\iota\kappa\mathbf{d}_k\cdot\mathbf{x}), \tag{20}$$

that approximates $K_{na}[u](\mathbf{x})$. Here $\mathbf{d}_k$ are unit vectors defining directions of wave propagation and $\psi = (\psi_1, \psi_2, \ldots, \psi_{n^{\text{wave}}})$ is a vector of expansion coefficients. Since $K_{na}[u](\mathbf{x})$ does not contain contributions from cells adjacent to $\mathbf{x}$, the expansion (20) converges exponentially fast with increasing number of wave vectors $\mathbf{d}_k$. The wave direction vectors $\mathbf{d}_k$ are chosen so that they sample the surface of the unit sphere with a sufficient degree of uniformity. The coefficients ψ_k, on the other hand, are chosen such that the expansion (20) matches the field values on the boundary of $\mathcal{C}_i$. The matching procedure thus requires solution of a system of linear equations

$$\mathbf{A}\psi = \mathbf{b}, \tag{21}$$

where the $n^{\text{face}} \times n^{\text{wave}}$-matrix $\mathbf{A}$ consists of elements $\exp(\iota\kappa\mathbf{d}\cdot\mathbf{x})$ evaluated at the equivalent-source points $\mathbf{x} = \mathbf{x}^l_{i,j}$ on the boundary of $\mathcal{C}_i$ and at the discrete direction vectors $\mathbf{d} = \mathbf{d}_k$. The right-hand side of Eq. (21), $\mathbf{b} = (b_1, b_2, \ldots, b_{n^{\text{face}}})$, is a vector of known values of $K_{na}[u]$ at all the equivalent-source points $\mathbf{x}^l_{i,j}$ on the boundary of $\mathcal{C}_i$. Again here, due to stability considerations, the problem is set up such that the associated linear system (21) is overdetermined.

Note that the identical geometry of cells $\mathcal{C}_i$ enables us to compute the QR-factorization of $\mathbf{A}$ only once and to store it for repeated use.

IV. ACCURACY AND EFFICIENCY

The above-presented integration schemes for computing adjacent and nonadjacent interactions are designed with the dual goal of achieving high order accuracy and computational efficiency. In this section we provide a brief summary of the arguments that substantiate these claims; numerical examples that further confirm these derivations are presented in Sec. V. Specifically, first, in Sec. IV A, we show that our numerical solution indeed converges to the exact solution with a tunable convergence order. In Sec. IV B then, we provide a derivation that delivers an optimal choice (to minimize computational effort) for the number L^3 of cells to be used in the acceleration procedure (cf. Sec. III B).

A. Accuracy: Error analysis

A careful derivation of an estimate for the error incurred by the algorithm presented in Sec. III can be performed in a rather straightforward manner, much as in other standard analyses of schemes for the solution of integral equations (see, e.g., Ref. 33). The basic estimate relates to that of the quadrature error, as an appeal to the uniform invertibility of the discretized operators then translates this into the actual error in the computed solution.

In our case, the quadrature error can be easily estimated, through bounds on the error incurred at each step of our procedure. Briefly, for instance, the error in the trapezoidal rule of steps 1 and 2 presented earlier is proportional to h_s^k where k denotes the degree of smoothness of the field *within* Ω, and h_s denotes the parallel grid spacing. Similarly, the error in the composite Newton-Cotes quadrature is no larger than a constant multiple of h_t^Q, where h_t is the grid size in the transverse direction. The error in the Fourier/polynomial interpolation of steps 3–5, on the other hand, is bounded by a constant times $(h_s/F)^R$ and, similarly, that in step 7 by h_t^R. The adjacent, parallel integration of steps 6 and 8, in turn, incur an error proportional to h_s^k and, finally, the transverse

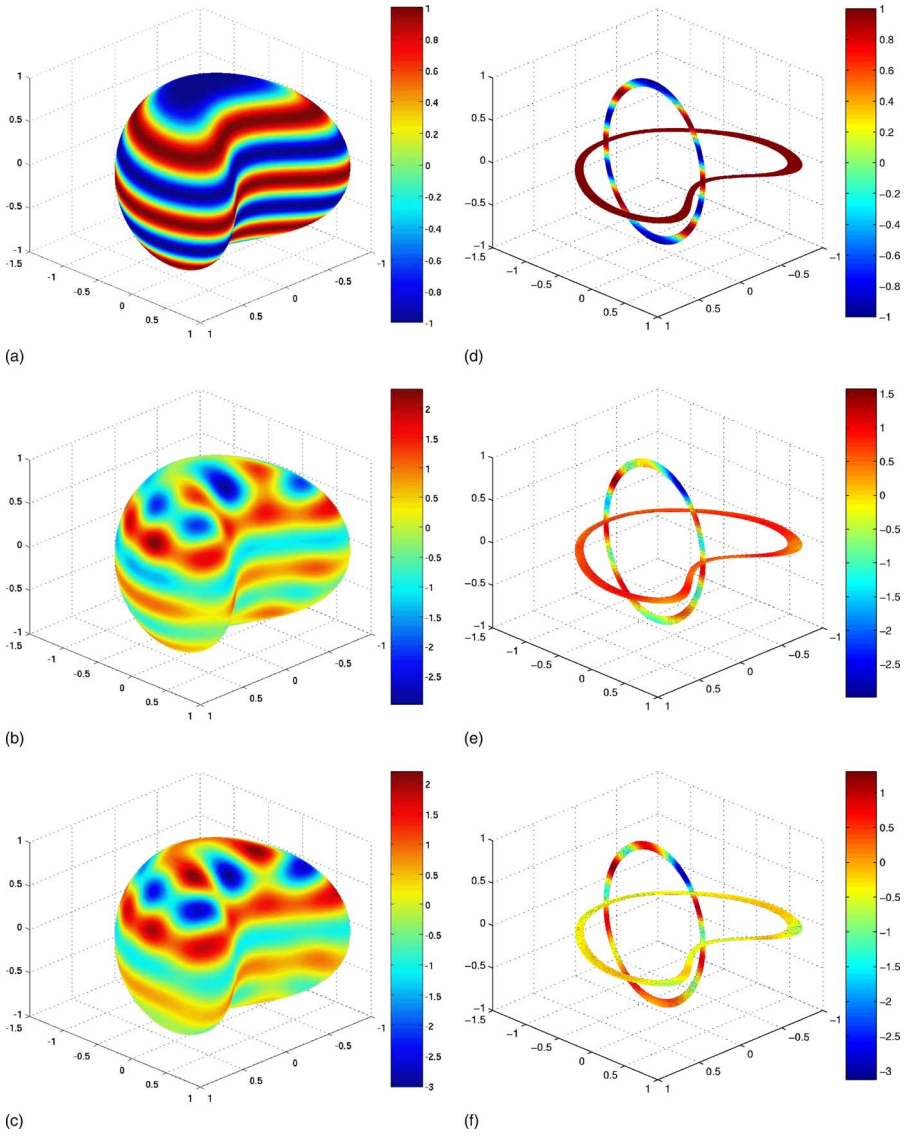

FIG. 5. (Color online) Scattering of an incoming plane wave by a bean-shaped thin scatterer. (a), (b), and (c) The surface view of the incident, total, and scattered field, respectively; (d), (e), and (f) the corresponding cross-sectional view.

integration in step 9 approximates the true value within $O(h_t^Q)$. Combining these observations, and letting F be such that $h_s/F < h_t$, we obtain

$$\text{Max Error} \leqslant \text{Const}(h_s^k + h_t^{\min(Q,R)}).$$

The above-presented analysis of the numerical scheme establishes the high-order convergence of the algorithm. The remaining issue of computational efficiency is analyzed in the following.

B. Efficiency: Operation count

The number of floating point operations required to compute $K[u]$ depends on L and M^{equiv} (cf. Sec. III B), in addition to the number N of volume discretization points. The latter must, of course, be chosen so as to correctly sample the field, on the scale of the wavelength of radiation, as well as to resolve material/geometrical variations. The number M^{equiv}, in turn, should guarantee that the equivalent field is also well-resolved. Since M^{equiv} is the number of points on a face of a cell $\mathcal{C}_i$, of area $(A/L)^2$, we must have

$$M^{\text{equiv}} \sim \kappa^2 A^2 / L^2. \tag{22}$$

The number L, on the other hand, is at our disposal and can therefore be chosen so to minimize the computational effort to attain a prescribed accuracy ϵ. To this end, we must evaluate the cost of each step of our procedure, as a function of L; the optimal choice then can be easily (and, explicitly) derived as that which minimizes the resulting overall cost.

To evaluate the cost of each step, we first note that, for a thin structure, only $\mathcal{O}(L/(\kappa A) \times L^2) = \mathcal{O}(L^3/(\kappa A))$ out of a total of L^3 cells $\mathcal{C}_i$ contain source points; the rest are empty. As a result,

$$\mathcal{O}(\kappa A N / L^3) \tag{23}$$

discretization points lie, on average, in each of the nonempty cells.

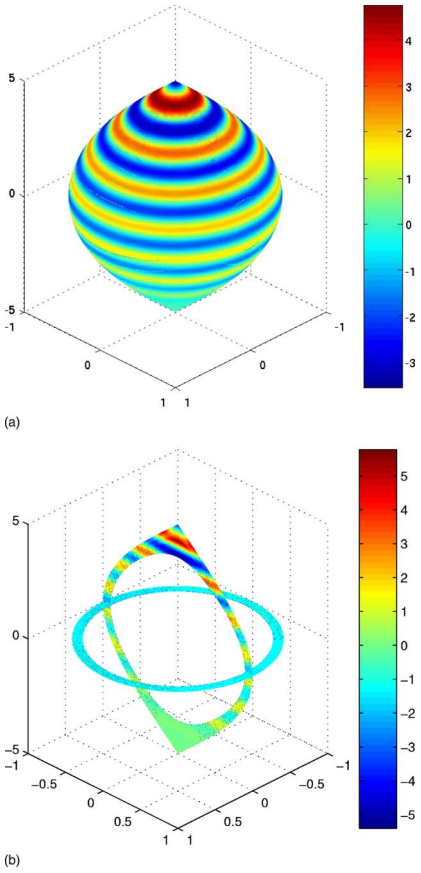

FIG. 6. (Color online) Scattering of an incoming plane wave by a thin scatterer with singularities. (a) and (b) The surface view and cross-sectional view of the computed scattered field, respectively, corresponding to an incident plane wave $\exp(\iota\kappa x_3)$ with $\kappa=5$.

Thus, the total number of operations required for the local integration (cf. Sec. III A) is as follows.

(1) Cost of adjacent integrations $=\mathcal{O}(N\times\kappa AN/L^3)$ $=\mathcal{O}(\kappa AN^2/L^3)$.

The interpolations necessary to allow for this integration (steps 3, 4, 5, and 7 in Sec. III A), on the other hand, cost no more than

(2) Cost of interpolation $=\mathcal{O}(N\log N)$ on account of the FFT refinement.

The cost of the acceleration scheme, finally, is largely determined by the need to perform three convolutions through FFTs on three-dimensional grids of size L^3M^{equiv} (L planes containing L^2M^{equiv} equivalent sources each).

(3) Cost of evaluation of equivalent source interactions $=\mathcal{O}(L^3M^{\text{equiv}}\log(L^3M^{\text{equiv}}))$.

In addition to this cost, we must also consider that of the corrections in Eq. (19) corresponding to cells $\mathcal{C}_i\subset\mathcal{S}_i$, and that of the least-squares problems that determine the equivalent sources and the coefficients of plane wave expansions [cf. Eq. (21)]. The former can be computed with three-dimensional FFTs of size M^{equiv} on each cell, for a total cost of

(4) Cost of corrections to equiv. source interactions $=\mathcal{O}((L^3/(\kappa A))M^{\text{equiv}}\log(M^{\text{equiv}}))$, while the latter demands the QR factorization of a single matrix of size M^{equiv} and the evaluation of the right-hand sides, for a cost of

(5) Cost of solution of (all) least-squares problems $=\mathcal{O}((M^{\text{equiv}})^3)+\mathcal{O}(NM^{\text{equiv}})$.

This last equality uses the fact that M^{equiv} is no bigger that the number of points per non-empty box [cf. Eq. (23)], which follows from Eq. (22) and the fact that N must be at least as large as the acoustic volume κ^2A^2 of the scatterer,

$$M^{\text{equiv}}\sim\mathcal{O}\left(\frac{\kappa A}{L}\frac{\kappa A}{L}\right)\leqslant\mathcal{O}\left(\frac{\kappa A}{L}\left(\frac{\kappa A}{L}\right)^2\right)$$
$$\leqslant\mathcal{O}\left(\frac{\kappa A}{L}\frac{N}{L^2}\right)=\mathcal{O}\left(\kappa A\frac{N}{L^3}\right). \tag{24}$$

Collecting these costs leads to an expression that, for each given N, can be minimized in L. A simple calculation then reveals that the optimal value of L is

$$L_{\text{opt}}=\begin{cases}\mathcal{O}(N^{(4-\beta)/8}) & \text{if } 4/5\leqslant\beta\leqslant 1\\ \mathcal{O}(N^{(4+\beta)/12}) & \text{if } \beta<4/5,\end{cases} \tag{25}$$

where

$$\beta(N,\kappa A)=\log(\kappa^2A^2)/\log(N) \tag{26}$$

is a relative measure of the refinement of the grid. With these choices we have

$$\text{Optimal Cost}=\begin{cases}\mathcal{O}(N^{(7\beta+4)/8}\log N) & \text{if } 4/5\leqslant\beta\leqslant 1\\ \mathcal{O}(N^{(\beta+4)/4}\log N) & \text{if } \beta<4/5.\end{cases} \tag{27}$$

Note that in the first case, corresponding to coarser discretizations, the operation count lies between $\mathcal{O}(N^{6/5}\log N)$ and $\mathcal{O}(N^{11/8}\log N)$. In the more relevant case of $\beta<4/5$, i.e., for more refined grids, the operation is lower and it approaches $N\log N$ with increasing refinement. In any case, as we said, the count is never higher than $\mathcal{O}(N^{11/8}\log N)$.

V. NUMERICAL RESULTS

In this section, we present numerical experiments for various thin structures in three dimensions. In all of the examples, the linear systems resulting from the discretization of Eq. (2) are solved by means of the iterative solver GMRES[34] in fully complex arithmetic.

The first example involves scattering computations for a thin spherical shell of refractive index $\sqrt{2}$ resulting from the incoming wave

$$u^i(\mathbf{x})=e^{\iota\kappa\mathbf{d}\cdot\mathbf{x}} \tag{28}$$

for which an exact solution can be computed. Four patches (see Fig. 2) were used to describe the thin spherical shell via smooth local parametrizations and the parameter values $F=4$, $Q=5$, and $R=4$ were used for the numerical computations. Recall that the parameter F is the level of refinement used in the trigonometric interpolation (steps 3 and 4), Q is the number of points used for the Newton-Cotes quadrature (steps 1, 2, and 9), and $R1$ is the degree of the interpolating polynomials (steps 5 and 7). The surface and cross-sectional views of the computed fields in the case $\mathbf{d}=(0,0,1)$ are presented in Fig. 3.

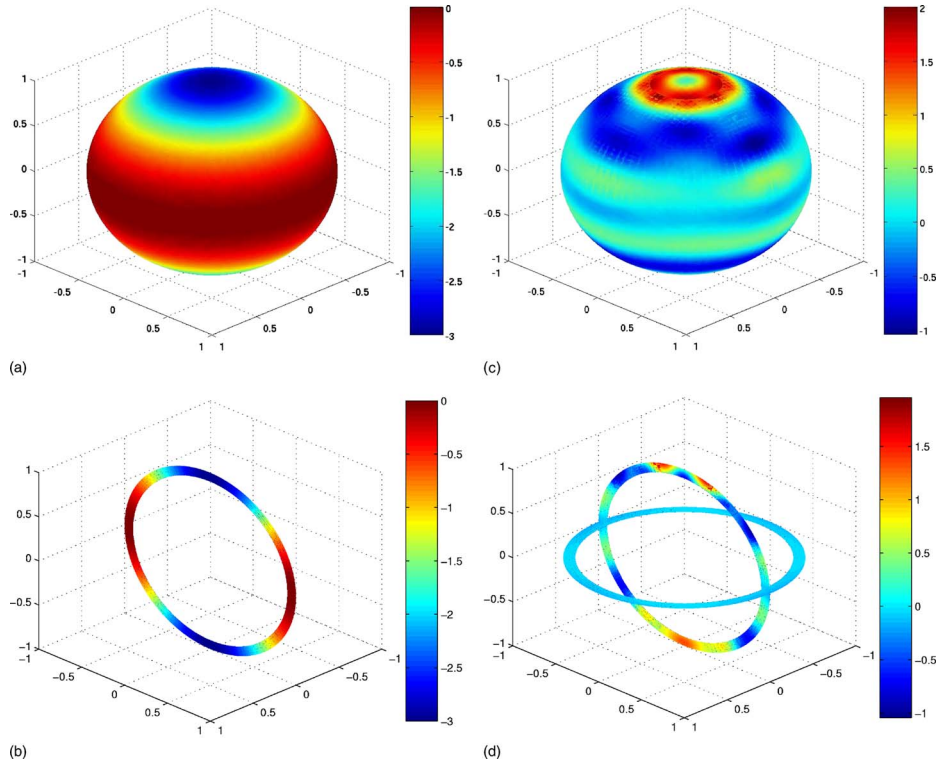

FIG. 7. (Color online) Variable index example. (a) and (b) The surface and cross-sectional views of the refractive index. (c) and (d) The surface view and cross-sectional view of the computed scattered field, respectively, corresponding to an incident plane wave $\exp(\iota\kappa x_3)$ with $\kappa=10$.

Numerical results on the maximum relative (near-field) error $\mathcal{E}$,

$$\mathcal{E} = \frac{\max_\Omega |u^{\text{exact}} - u^{\text{computed}}|}{\max_\Omega |u^{\text{exact}}|},$$

for the example of Fig. 3 are presented in Table I. Clearly, these results confirm the high-order convergence of the scheme (cf. Sec. IV A). In Table II, on the other hand, we present a numerical study of the computational complexity associated with this example. To this end we consider a sequence of scattering problems with increasing frequencies and wherein the thickness of the domain is correspondingly reduced so as to continue to satisfy the thinness assumption (4). Table II shows that the computational effort grows as predicted by Eq. (27). To display this, the growth in the computational cost for successive doublings of the wave number, and consequent quadrupling of the number of points, is measured by

$$\mathcal{R} = \frac{(T_{2\kappa}/\log 4N)^{1/q_{2\kappa}}}{(T_\kappa/\log N)^{1/q_\kappa}}.$$

Here T_κ and $T_{2\kappa}$ are the computational times corresponding to κ and 2κ, respectively, and $q_\kappa=(4+\beta_\kappa)/4$ and $q_{2\kappa}=(4+\beta_{2\kappa})/4$ denote the powers in the count (27). As predicted the ratios $\mathcal{R}$ do not exceed 4, the ratio of the number of points.

Our algorithm, of course, is not constrained by the geometry of the scattering object. In fact, the only requirement to handle any given geometry is that suitable local parametrizations be constructed. To demonstrate this, we present two additional examples involving a bean-shaped thin scatterer and a thin volume geometry with conic singularities, with $n^2=2$. The former geometry corresponds to the parametrization

TABLE III. (a) Maximum relative near field error (as compared with the analytical solution) for the scattering configuration in Fig. 8 with N discretization points. (b) Computational time per iteration for incident plane waves of increasing frequency (and corresponding increases in the number of unknowns).

(a)				(b)			
N	Samp. density[a]	Max error	Order	κa	N	Time/iter. (s)	Order
3×16^2	4	2.3795$E-1$		4	3×32^2	7	
3×32^2	8	1.8715$E-3$	6.99	8	3×64^2	35	1.2
3×64^2	16	2.6252$E-5$	6.16	16	3×128^2	151	1.1
3×128^2	32	1.3674$E-7$	7.58	256	3×256^2	688	1.1

[a]Number of points per wavelength

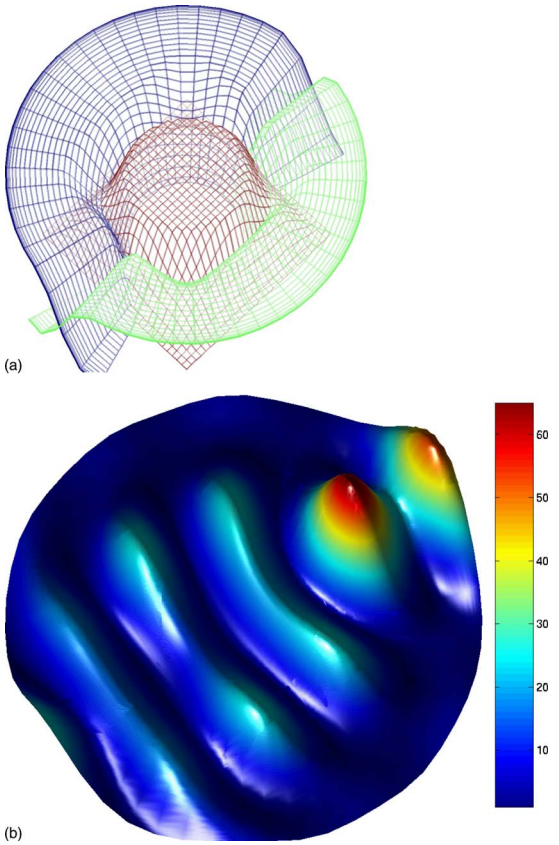

FIG. 8. (Color online) (a) The decomposition of an inhomogeneity (a circular cylinder with radius a and constant refractive index $n=2$) into two thin-volume patches and one bulk patch, with the associated discretization mesh. (b) The near field intensity of the solution u due to an incident plane wave traveling from lower-left to upper-right with $\kappa a=4$.

$$\frac{x_1^2}{a^2}+\frac{\left(\alpha_1 A\cos\frac{\pi x_1}{A}+x_2\right)^2}{b^2\left(1-\alpha_2\cos\frac{\pi x_1}{A}\right)}+\frac{x_3^2}{c^2\left(1-\alpha_3\cos\frac{\pi x_1}{A}\right)}=A^2(1-Bt)^2$$

with $a=1.0$, $b=1.0$, $c=1.0$, $\alpha_1=0.3$, $\alpha_2=0.4$, $\alpha_3=0.1$, $A=1.0$, $B=0.1$, and $0\leqslant t\leqslant 1$ (see Fig. 4). The field computations for this configuration [$\kappa=10$, $\mathbf{d}=(0,0,1)$] are presented in Fig. 5. Results for the singular geometry

$$x_1^2+x_2^2+\sin^2\left(\frac{\pi x_3}{2c}\right)=(1-Bt)^2$$

with $c=5.0$, $B=0.1$, and $0\leqslant t\leqslant 1$, in turn, are presented in Fig. 6 [$\kappa=5$, $\mathbf{d}=(0,0,1)$].

By design, our algorithm is also not restricted to consideration of constant or piecewise constant refractive indices. An example with variable refractive index is included in Fig. 7 for a spherical shell scatterer. The refractive index is given by

$$n(r,\phi,\theta)=1+\cos^2\theta$$

and the incidence is a plane wave with $\kappa=10$ and $\mathbf{d}=(0,0,1)$.

VI. DISCUSSION

Our present work concentrates on the specialized treatment of regions near material discontinuities, which we view as thin scatterers. Here, however, we briefly discuss the application of these ideas to the general case, wherein we couple our new schemes to the more classical approaches, such as those described in Ref. 26, to deliver fast and accurate solutions in the presence of discontinuities. The basic premise here is that, as we mentioned, these latter spectral methodologies deliver highly accurate solutions whenever the scattering media vary smoothly. In Fig. 8 we display some preliminary results of the integration of the spectral scheme proposed in Ref. 26 with our new thin-volume scattering solver. Figure 8(a) shows the "partition of unity" used here to smoothly separate the "bulk" of the domain, to be treated with the method of Ref. 26, from the thin "boundary volumes" to which the schemes presented in this text are applied. The interaction between the bulk and boundary volumes are effected via FFTs and equivalent source calculations (see Sec. III B). Table III, on the other hand, shows that high-order accuracy is indeed attained, and that the cost grows only linearly with problem size. A thorough analysis and further applications of such integrated algorithms, however, are left for future work.

The numerical experiments indicate that the number of iterations required by GMRES to solve the linear system arising from the discretized integral equation, without any preconditioning, increases quadratically with the problem size (e.g., κa). For example, 23 iterations were needed in the above-presented example for $\kappa a=4$. Although a considerable research effort has been devoted to the development of effective preconditioning techniques for such scattering problems,[35,36] it still cannot be considered completely solved and remains the subject matter of much ongoing research.

VII. CONCLUSIONS

We have presented a numerical scheme for scalar thin-structure scattering simulations that can deliver highly accurate results with a reduced operation count. The method is based on an accurate numerical representation of the singular operators that arise in the integral equation formulation and on FFT-accelerated evaluations. The former are attained through specialized high-order quadratures, while the latter rely on the evaluation of equivalent sources on Cartesian grids.

The theoretical and numerical results presented here demonstrate the viability of the approach in the context of acoustic scattering off thin structures that may be of independent interest (e.g., material coatings). As follows from our discussion, however, the basic ideas behind our schemes can be readily extended to other wave models (electromagnetics, elasto-dynamics). More importantly perhaps, we have also explained how our new algorithms can provide an effective means to upgrade existing FFT-based numerical methods to allow these to accurately handle material discontinuities, by smoothly separating the scatterer into an interior bulk and thin boundary volumes. Indeed, as we said, any method that can efficiently and accurately compute the scatter off

smoothly varying media can be used to treat the bulk, and interfaced with the thin volume solver presented here to compute the fields in the vicinity of discontinuities. As we have shown, this interface can be made seamless and in a manner that provides high-order convergence without compromising efficiency.

ACKNOWLEDGMENTS

F.R. gratefully acknowledges support from AFOSR through Contract No. FA9550-05-1-0019, from NSF through Grant No. DMS-0311763, and from the Army High Performance Computing Research Center (AHPCRC) under Army Research Laboratory Cooperative Agreement No. DAAD19-01-2-0014. The computations for this project were carried out at the Minnesota Supercomputing Institute, whose support is also gratefully acknowledged.

[1]G. Cohen and P. Joly, "Construction and analysis of fourth order finite difference schemes for the acoustic wave equations in nonhomogeneous media," SIAM (Soc. Ind. Appl. Math.) J. Numer. Anal. **33**, 1266–1302 (1996).

[2]A. Bamberger, R. Glowinski, and Q. H. Tran, "A domain decomposition method for the acoustic wave equation with discontinuous coefficients and grid change," SIAM (Soc. Ind. Appl. Math.) J. Numer. Anal. **34**, 603–639 (1997).

[3]B. Gustafsson and P. Wahlund, "Time compact difference methods for wave propagation in discontinuous media," SIAM J. Sci. Comput. (USA) **26**, 272–293 (2004).

[4]A. Kirsch and P. Monk, "Convergence analysis of a coupled finite-element and spectral method in acoustic scattering," IMA J. Numer. Anal. **10**, 425–447 (1990).

[5]W. Rachowicz and L. Demkowicz, "An hp-adaptive finite element method for electromagnetics. 1. Data structure and constrained approximation," Comput. Methods Appl. Mech. Eng. **187**, 307–335 (2000).

[6]A. Kirsch and P. Monk, "An analysis of the coupling of finite-element and nystrom methods in acoustic scattering," IMA J. Numer. Anal. **14**, 523–544 (1994).

[7]Q. H. Liu, "Large scale simulations of electromagnetic and acoustic measurements using the pseudospectral time-domain method (pstd) algorithm," IEEE Trans. Geosci. Remote Sens. **37**, 917–226 (1999).

[8]B. Yang, D. Gottlieb, and J. S. Hesthaven, "Spectral simulations of electromagnetic wave scattering," J. Comput. Phys. **134**, 216–230 (1997).

[9]Q. H. Liu, "The pseudospectral time-domain (pstd) algorithm for acoustic waves in absorptive media," IEEE Trans. Ultrason. Ferroelectr. Freq. Control **45**, 1044–1055 (1998).

[10]T. D. Mast, L. P. Souriau, D. L. D. Liu, M. Tabei, A. I. Nachman, and R. C. Waag, "A k-space method for large scale-models of wave propagation in tissue," IEEE Trans. Ultrason. Ferroelectr. Freq. Control **48**, 341–354 (2001).

[11]M. Tabei, T. D. Mast, and R. C. Waag, "A k-space method for coupled first-order acoustic propagation equations," J. Acoust. Soc. Am. **111**, 53–63 (2002).

[12]N. N. Bojarski, "The k-space formulation of the scattering problem in the time domain," J. Acoust. Soc. Am. **72**, 570–884 (1982).

[13]N. N. Bojarski, "The k-space formulation of the scattering problem in the time domain: An improved single propagator formulation," J. Acoust. Soc. Am. **77**, 826–831 (1985).

[14]J. Lu, J. Pan, and B. Xu, "Time-domain calculation of acoustical wave propagation in discontinuous media using acoustical wave propagator with mapped pseudospectral method," J. Acoust. Soc. Am. **118**, 3408–3419 (2005).

[15]A. Dutt and V. Rokhlin, "Fast Fourier transform for nonequispaced data," SIAM J. Sci. Comput. (USA) **14**, 1368–1393 (1993).

[16]N. Nguyen and Q. H. Liu, "The regular Fourier matrices and non-uniform fast Fourier transforms," SIAM J. Sci. Comput. (USA) **21**, 283–293 (1999).

[17]Q. H. Liu, X. M. Xu, B. Tian, and Z. Q. Zhang, "Applications of nonuniform fast Fourier transform algorithms in numerical solutions of differential and integral equations," IEEE Trans. Geosci. Remote Sens. **38**, 1551–1560 (2000).

[18]D. Gottlieb, C. W. Shu, A. Solomonoff, and H. Vandeven, "On the Gibbs phenomenon. i. Recovering exponential accuracy from the Fourier partial sum of a nonperiodic analytic function," J. Comput. Appl. Math. **43**, 81–98 (1992).

[19]S. A. Sarra, "Spectral methods with postprocessing for numerical hyperbolic heat transfer," Numer. Heat Transfer, Part A **43**, 717–730 (2003).

[20]J. P. Boyd, "Trouble with Gegenbauer reconstruction for defeating Gibbs' phenomenon: Runge phenomenon in the diagonal limit of Gegenbauer polynomial approximations," J. Comput. Phys. **204**, 253–264 (2005).

[21]X. M. Xu and Q. H. Liu, "Fast spectral method for acoustic scattering problems," IEEE Trans. Ultrason. Ferroelectr. Freq. Control **48**, 522–529 (2001).

[22]P. Zwamborn and P. D. van den Berg, "The three-dimensional weak form of the conjugate gradient fft method for solving scattering problems," IEEE Trans. Microwave Theory Tech. **40**, 1757–1766 (1992).

[23]G. X. Fan and Q. H. Liu, "The CGFFT method with a discontinuous FFT algorithm," Microwave Opt. Technol. Lett. **29**, 47–49 (2001).

[24]G. Liu and S. D. Gedney, "High-order nystrom solution of the volume—efie for te-wave scattering," Electromagnetics **21**, 1–13 (2001).

[25]A. Zhu and S. D. Gedney, "A quadrature-sampled pre-corrected FFT method for the electromagnetic scattering from inhomogeneous objects," IEEE Antennas Wireless Propag. Lett. **2**, 50–53 (2003).

[26]E. M. Hyde and O. P. Bruno, "A fast, higher-order solver for scattering by penetrable bodies in three dimensions," J. Comput. Phys. **202**, 236–261 (2005).

[27]D. Colton and R. Kress, *Inverse Acoustic and Electromagnetic Scattering Theory*, 2nd ed. (Springer, Berlin, 1998).

[28]P. Werner, "Zur mathematischen theorie akustischer wellenfelder (On the mathematical theory of acoustic wave fields)," Arch. Ration. Mech. Anal. **6**, 231–260 (1960).

[29]P. Werner, "Beugungsprobleme der mathematischen akustik (Diffraction problems of mathematical acoustics)," Arch. Ration. Mech. Anal. **12**, 155–184 (1963).

[30]P. A. Martin, "Acoustic scattering by inhomogeneous obstacles," SIAM J. Appl. Math. **64**, 297–308 (2003).

[31]O. P. Bruno and L. A. Kunyansky, "A fast, high-order algorithm for the solution of surface scattering problems: Basic implementation, tests and applications," J. Comput. Phys. **169**, 80–110 (2001).

[32]L. B. Felsen and N. Markuvitz, *Radiation and Scattering of Waves* (Prentice-Hall, New York, 1973).

[33]R. Kress, *Linear Integral Equations* (Springer, Berlin, 1989).

[34]Y. Saad and M. H. Schultz, "Gmres: A generalized minimal residual algorithm for solving non-symmetric linear systems," SIAM (Soc. Ind. Appl. Math.) J. Sci. Stat. Comput. **7**, 856–869 (1986).

[35]J. Lee, J. Zhang, and C. C. Lu, "Incomplete Lu preconditioning for large scale dense complex linear systems from electromagnetic wave scattering problems," J. Comput. Phys. **185**, 158–175 (2003).

[36]E. M. Hyde and O. P. Bruno, "An efficient, preconditioned, high-order solver for scattering by two-dimensional inhomogeneous media," J. Comput. Phys. **200**, 670–694 (2004).